

Targeting Tumor-Associated Exosomes with Integrin-Binding Peptides

Randy P. Carney,* Sidhartha Hazari, Tatu Rojalin, Alisha Knudson, Tingjuan Gao, Yuchen Tang, Ruiwu Liu, Tapani Viitala, Marjo Yliperttula, and Kit S. Lam*

All cells expel a variety of nanosized extracellular vesicles (EVs), including exosomes, with composition reflecting the cells' biological state. Cancer pathology is dramatically mediated by EV trafficking via key proteins, lipids, metabolites, and microRNAs. Recent proteomics evidence suggests that tumor-associated exosomes exhibit distinct expression of certain membrane proteins, rendering those proteins as attractive targets for diagnostic or therapeutic application, yet it is not currently feasible to distinguish circulating EVs in complex biofluids according to their tissue of origin or state of disease. Here, peptide binding to tumor-associated EVs via overexpressed membrane protein is demonstrated. It is found that SKOV-3 ovarian tumor cells and their released EVs express $\alpha_3\beta_1$ integrin, which can be targeted by the in-house cyclic nonapeptide, LXY30. After measuring bulk SKOV-3 EV association with LXY30 by flow cytometry, Raman spectral analysis of laser-trapped single exosomes with LXY30-dialkyne conjugate enables the differentiation of cancer-associated exosomes from noncancer exosomes. Furthermore, the foundation for a highly specific detection platform for tumor-EVs in solution with biosensor surface-immobilized LXY30 is introduced. LXY30 not only exhibits high specificity and affinity to $\alpha_3\beta_1$ integrin-expressing EVs, but also reduces EV uptake into SKOV-3 parent cells, demonstrating the possibility for therapeutic application.

at an advanced stage. Fortunately, all cells expel extracellular vesicles (EVs), whose biomolecular contents reflect the composition and state of their parent cells.^[2] A nanosized subset of these vesicles, termed exosomes, holds great promise for cancer diagnostics, and can be detected in numerous biofluids, including blood, urine, saliva, ascites, and cerebrospinal fluid.^[3–5]

Tumor cells can hijack the exosomal pathway for means of immunosuppression, antigen presentation, tumor growth, and metastasis.^[6–9] It has been demonstrated that proteins, genes, lipids, and metabolites exhibit distinct profiles within exosomes derived from tumor cells compared to healthy cells.^[10,11] Combined with the cell's ability to quickly alter EV composition in response to stimulus (e.g., stress, pathology, and drug treatment), exosomes have been implicated as vast mediators of intercellular communication, and provide a framework for diagnostic platform development. Much work is currently

underway to develop methods for exploiting the chemical content trafficked in tumor-associated exosomes for use as potent biomarkers.^[12–17]

An ideal point-of-care isolation strategy for cancer diagnostics would address two issues: first, tumor-associated EV subpopulations represent only a small fraction of the circulating secretome, thus the nontumor EV background impedes sensitive detection. Second, tumor EVs should be distinguished

1. Introduction

For the past two decades, the mortality rate has steadily declined for certain cancers (lung, prostate, colon, and breast), yet has changed very little for others (ovarian, pancreatic, liver, stomach, uterine, leukemia, and bladder).^[1] The latter group suffers a notable lack of noninvasive early detection methodologies, leaving few treatment options for patients diagnosed

Dr. R. P. Carney, Dr. S. Hazari, A. Knudson, Dr. R. Liu, Prof. K. S. Lam
Department of Biochemistry and Molecular Medicine
School of Medicine
University of California Davis
Sacramento, CA 95817, USA
E-mail: randycarney@icloud.com; kslam@ucdavis.edu


Dr. T. Rojalin, Dr. T. Viitala, Prof. M. Yliperttula
Division of Pharmaceutical Biosciences
Centre for Drug Research
University of Helsinki
Helsinki 00014, Finland

Dr. T. Rojalin, Dr. T. Gao, Dr. Y. Tang
Center for Biophotonics
University of California Davis
Sacramento, CA 95817, USA

Dr. T. Gao, Dr. Y. Tang
College of Chemistry
Central China Normal University
Wuhan 430079, China

Prof. M. Yliperttula
Department of Pharmaceutical Sciences
University of Padova
Padua 35131, Italy

Prof. K. S. Lam
University of California Davis Comprehensive Cancer Center
Sacramento, CA 95817, USA

 The ORCID identification number(s) for the author(s) of this article can be found under <http://dx.doi.org/10.1002/adbi.201600038>.

DOI: 10.1002/adbi.201600038

from nontumor EVs. One potential approach for simple, rapid discrimination of tumor EVs is to exploit differences in their surface composition. Many membrane proteins have been identified to be generally associated with exosome-type EVs (CD9, CD63, CD81, and EpCAM).^[18] Others have been reported to be enriched in certain tumor-associated exosomes, such as EGFR and HER2.^[19,20] Given that several recent studies have demonstrated enrichment of particular integrins in exosomes derived from a variety of tumor cells, exosomal integrins are interesting potential targets.^[21–26]

Integrins are transmembrane heterodimer glycoproteins composed of an α and β subunit, and contribute to a variety of normal and pathogenic biological processes including cell adhesion, inflammation, thrombosis, metastasis, and adhesion-mediated drug resistance.^[27] Characteristic combinations of integrins are often overexpressed in certain tumor cells.^[27] In 2015, Hoshino et al. described that organotropic tumor metastasis is largely mediated via exosomal integrin trafficking.^[9] They demonstrated that exosomes expressing integrins $\alpha_6\beta_4$ and $\alpha_6\beta_1$, or $\alpha_v\beta_5$, contributed to metastatic spreading toward the lung or liver, respectively, and that prior “education” with lung-tropic exosomes (by retro-orbital injection in mice) redirected metastasis of bone-tropic tumor cells to the lung.^[9] Furthermore, targeting of the $\alpha_6\beta_4$ or $\alpha_v\beta_5$ integrins decreased metastasis.^[9] Thus, EV-expressed integrins represent an attractive target for both (i) diagnostic discrimination of circulating tumor EVs and (ii) therapeutic application by binding tumor EV integrins in order to block their tumorigenic function.

Recent work in our lab has led to the discovery of several unique ligands capable of binding tumor cells through their overexpressed integrins, including ligands against $\alpha_3\beta_1$,^[28,29] $\alpha_4\beta_1$,^[30] and $\alpha_v\beta_3$.^[31] These ligands were found by screening tumor cells against focused combinatorial libraries of peptide or peptidomimetic molecules, via the one-bead one-compound (OBOC) combinatorial library approach.^[32,33] One motif in particular, [c(d/D)GXGXXc] (where d-amino acids are lowercase and X represents a randomized position), generated several lead peptide ligands with specific binding to $\alpha_3\beta_1$ integrin-expressing ovarian adenocarcinoma, glioblastoma, and metastatic breast cancer.^[28] The best of these lead ligands, termed LX1 [cdGLG-Hyp-Nc] (where Hyp is

hydroxyproline),^[29] was further optimized through structure–activity relationship studies and a more focused OBOC combinatorial library. This generated the highly potent cyclic disulfide-containing peptide: LX130 [cdG-Phe(3,5-diF)-G-Hyp-NcR].^[34] LX130 showed increased in vitro and in vivo tumor targeting across a panel of ovarian, breast, brain, and nonsmall-cell lung carcinoma (NSCLC) cells. Furthermore, the binding specificity of LX130 to the α_3 integrin subunit was confirmed, since binding to α_3 -expressing U-87MG cells could be inhibited by preincubation of the cells with anti- α_3 antibody.^[34] Finally, a scrambled version of LX130 (scr-LX130: [cGd-Hyp-Phe(3,5-diF)-G-NcR]), featuring switched positions of some amino acids in the peptide sequence, did not significantly bind to $\alpha_3\beta_1$ integrin-expressing cells, demonstrating the sequence specificity of LX130.^[34]

Here, we describe the characterization of the $\alpha_3\beta_1$ integrin-binding peptide LX130 with respect to binding exosomes derived from $\alpha_3\beta_1$ -expressing ovarian tumor cells. Through a combination of bulk and single EV characterization techniques, we demonstrate that LX130 exhibits high binding affinity to specific tumor cell-derived exosomes, likely via the overexpressed $\alpha_3\beta_1$ integrin.

2. Results

2.1. Exosome Isolation and Characterization

Exosomes isolated from SKOV-3 ovarian tumor cells overexpressing $\alpha_3\beta_1$ integrin, Jurkat leukemia cells overexpressing $\alpha_4\beta_1$ integrin, and healthy human plasma were compared in this study. Classic ultracentrifugation (UC) methodology was used to isolate EVs from both cancer cell culture supernatant (see the Experimental Section for full detail) and human plasma samples.^[35] The collected EVs were confirmed as exosomes by employing the International Society for Extracellular Vesicles (ISEV) suggested standards^[36] for minimal characterization (**Figure 1**). Thus, western blot (WB) supported both the presence of multivesicular body-associated proteins CD63, CD9, and tsg101, and also the absence of endoplasmic reticulum-associated protein calnexin (Figure 1a). Imaging by

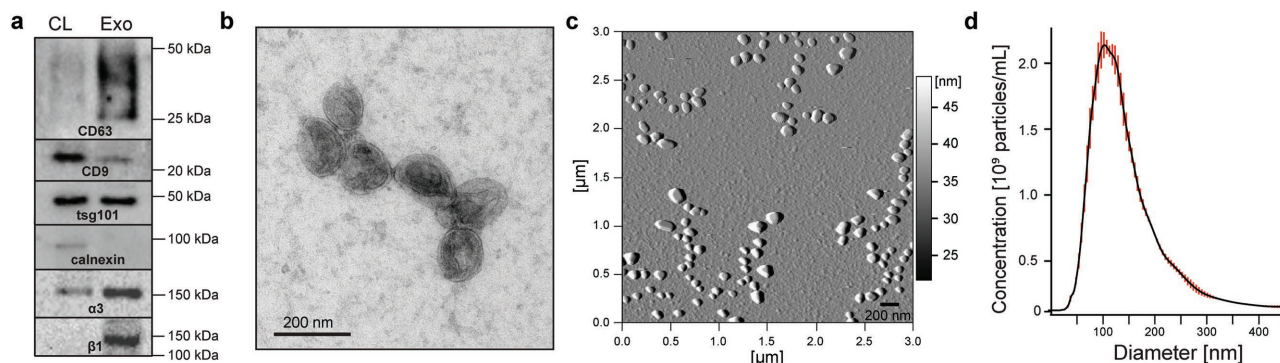


Figure 1. Confirmation of exosome type for vesicles isolated from SKOV-3 ovarian tumor cells. a) Western blot analysis for CD63, CD9, tsg101, calnexin, and α_3 and β_1 integrin subunits in SKOV-3 cell lysate (CL) and exosome (Exo) preparations (20 μ g protein per lane). b) Electron microscopy image of exosomes by negative-stained conventional EM showing the typical cup-shaped morphology. c) AFM amplitude image of isolated exosomes deposited on mica. d) Exosome number concentration and size distribution by NTA, with red bars representing one standard deviation.

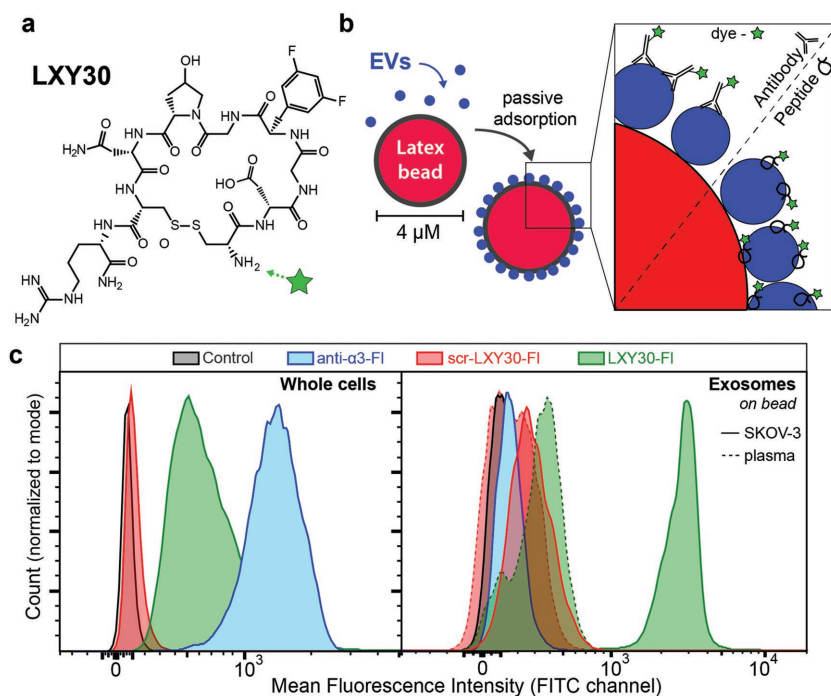


Figure 2. On-bead flow cytometry (FC). a) Chemical structure of the LXLY30 peptide. For FC measurement, the N-terminus of the peptide is coupled to a FITC dye molecule via PEGylated spacer. b) Exosomes tagged with fluorescently labeled antibody or peptide are bound to sulfate/aldehyde-coated latex beads for FC measurement. c) FC profiles of fluorescence-labeled LXLY30 (green), scr-LXY30 (red), and anti- α_3 (blue) binding to SKOV-3 cells (left) or exosomes (right). Exosomes from healthy human plasma showed limited binding to scr-LXY30 (dotted red) and LXLY30 (dotted green).

negative-stained electron microscopy (EM) demonstrated typical exosome size and “cup-shape” morphology (Figure 1b).^[36] Atomic force microscopy (AFM) provided complementary size measurement (Figure 1c). Nanoparticle tracking analysis (NTA) was used to determine EV concentration ($1.70 \pm 0.11 \times 10^{13}$ particles mL^{-1}) and size distribution (177 ± 87 nm) (Figure 1d). According to a recently reported metric to assess exosome purity, we measured the ratio of protein concentration to particle number concentration to be 2.6×10^9 particles μg^{-1} protein, confirming that our isolation procedure reliably purified exosomes from excessive protein contamination.^[37]

2.2. On-Bead Flow Cytometry

To confirm cell–peptide binding, LXLY30 (Figure 2a) and scr-LXY30 were labeled with fluorescein isothiocyanate (LXY30-FI) dye via PEG₂ spacer at the peptide N-terminus and incubated with SKOV-3 cells. As previously reported, SKOV-3 cells exhibited high affinity for LXLY30-FI but only minimal affinity for the scrambled analogue (Figure 2c, left panel).^[34] Next, SKOV-3 exosomes were premixed with either LXLY30-FI or scr-LXY30-FI overnight. After purification from unbound ligand by centrifugal filtration, exosomes were mixed with the latex beads (Figure 2b). Similar to the cells, flow cytometry revealed a significant increase in fluorescence intensity for exosomes bound to LXLY30-FI compared to the scrambled-LXY30-FI (Figure 2c, right panel) (statistical significance of $p < 0.01$). On the other

hand, $\alpha_4\beta_1$ -expressing Jurkat tumor cells and their released exosomes bound LXLY30-FI and scr-LXY30-FI to a similar, minimal extent (data not shown). When incubated with anti- α_3 -FI, SKOV-3 cells demonstrated a high degree of binding, yet bead-bound SKOV-3 exosomes showed little increase in fluorescence compared to the control. In addition to the Jurkat cell-derived exosome control that tested the specificity of our peptide LXLY30 toward its expected $\alpha_3\beta_1$ integrin target, we also tested exosomes isolated from healthy human plasma samples. Following ultracentrifugation isolation (see the Experimental Section for full detail), the plasma-derived exosomes were subjected to LXLY30-FI and scr-LXY30-FI binding and examination by on-bead flow cytometry (Figure 2c, dotted lines). The healthy human-plasma-derived exosomes did not exhibit significant binding to either LXLY30-FI or scr-LXY30-FI peptide.

On-bead flow cytometry is limited to measuring bulk exosomes, and therefore may not be sensitive enough to distinguish circulating tumor-associated EVs. While single exosome flow cytometry is becoming feasible, it is still presently too unreliable for timely reporting of our findings. We therefore developed a new Raman spectroscopic method to measure LXLY30-exosome binding for single vesicles.

2.3. Laser Tweezers Raman Spectroscopy (LTRS)

We employed LTRS to measure the binding of LXLY30 to single vesicles by analyzing variations in Raman-active peaks for optically trapped vesicles, via adaptation of our previously reported methodology for single vesicle LTRS.^[38] As the ISEV-suggested characterization framework^[36] becomes more difficult to apply on a single-vesicle basis, here we refer to the optically trapped vesicles more generally as EVs.

For determining the extent of ligand binding to single EVs, LXLY30 and scr-LXY30 peptides were each covalently functionalized with a highly Raman-active compound: 4-(phenylbuta-1,3-dien-1-yl)benzoic acid (RT, for Raman Tag). In a region typically empty of Raman chemical shifts for unlabeled EVs, the di-alkyne and aromatic bonds present in the RT give rise to strong Raman shifts at 1600 and 2230 cm^{-1} , respectively (Figure 3, blue trace). EV samples were incubated with LXLY30-RT or scr-LXY30-RT (1×10^{-6} M) for optical tweezers trapping and Raman spectra measurement by LTRS. For each condition, at least ten individual EVs with sizes in the range of 80–200 nm were trapped and their Raman spectra averaged over 5 min. Typical peaks were indicative of EV trapping, for example, the peak centered at 1066 cm^{-1} can be assigned to C–C stretching in lipids, the peak at 1450 cm^{-1} assigned to CH₂ and CH₃ deformations in proteins and lipids, and the peaks at 1651 and 1668 cm^{-1} as C=C stretching in lipids and protein amide

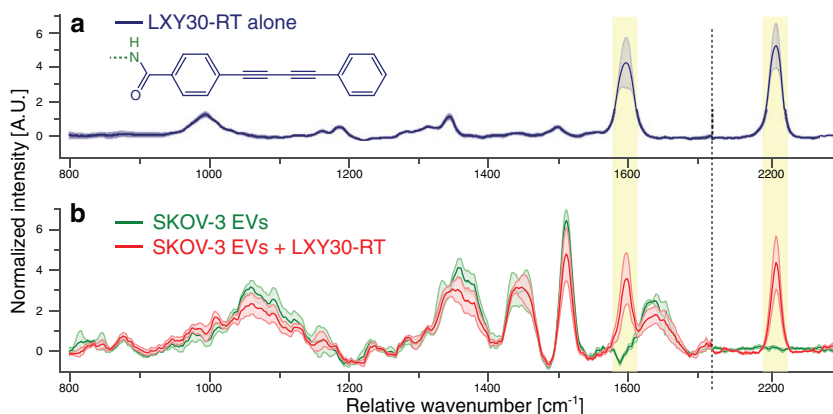


Figure 3. Laser tweezers Raman spectroscopy (LTRS) of SKOV-3 EV binding to Raman-tagged LXY30. Top: Normalized Raman spectra for LXY30-RT peptide. Bottom: Raman spectra for SKOV-3 EVs before (green) and after (red) LXY30-RT addition. When the spectra are overlaid, two prominent peaks indicative of the chemical shifts for the Raman tag become apparent (highlighted in yellow). The solid line and shaded area represent the average \pm one standard deviation.

I vibrations, respectively.^[38] Effectively at the same dilution, the LXY30-RT peptide alone was undetectable (the spectra presented in Figure 3a are far more concentrated), yet when condensed on the vesicle could be observed quite strongly, as evident by the emergence of the two characteristic RT peaks (Figure 3b). Incubation with scr-LXY30-RT resulted in little discernible binding, and furthermore control Jurkat exosomes, which lack $\alpha_3\beta_1$, were not detected to measurably bind LXY30-RT. For trapped exosomes isolated from healthy human plasma, too, we could not detect any binding to LXY30-RT or scr-LXY30-RT. To quantify the relative binding stoichiometry of LXY30-RT to a single SKOV-3 vesicle, we further examined the region between 1550 and 1700 cm^{-1} (Figure 4). This region contains two major peaks, Peak A, centered at 1600 cm^{-1} arising from

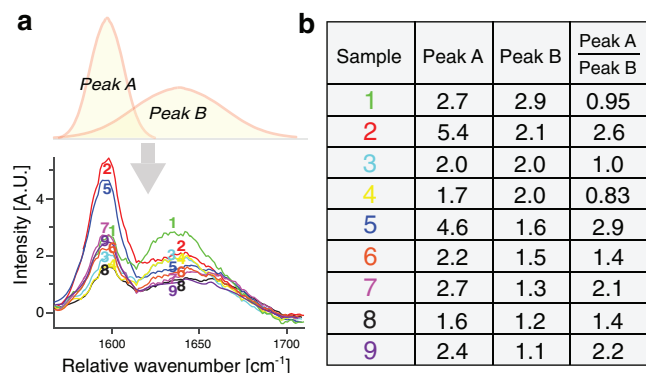


Figure 4. a) Representative Raman spectra (without normalization) for single vesicles mixed with LXY30-RT peptide. In this wavenumber region, peaks originate either from the LXY30-RT (centered near 1600 cm^{-1}) or from the exosomal contents (amide region centered near 1650 cm^{-1}). Spectra are colored and numbered for ease in comparison. Gaussian curve fitting was used to distinguish peak A from peak B and obtain peak heights (e.g., spectra no. 2 is plotted above the raw data). b) Measured heights of peak A and peak B for each spectrum, and their ratios, listed in descending order by peak B height. The ratios are not constant, indicating that stoichiometry may not be fixed across exosome size as might be expected, and moreover varies widely from vesicle to vesicle.

the Raman tag's aromatic/di-alkyne functional group, and Peak B, the group of peaks arising from the aforementioned exosome protein/lipid content. The ratio of these peaks was taken for absolute comparison of chemical contribution from either the RT or the exosome. For this comparison, the Raman intensities were not normalized. We observed that the peaks did not scale together (Figure 4b), indicating that total protein content and LXY30 binding were not linearly correlated.

2.4. Effect of LXY30-Binding on Cell Uptake

Following demonstration of specific binding of LXY30 peptide to SKOV-3 cells and their derived exosomes, we tested whether LXY30-binding could inhibit or otherwise affect cell uptake of SKOV-3 exosomes. For visualization by confocal laser scanning microscopy (CLSM), isolated SKOV-3 exosomes were nonspecifically labeled with the red fluorescent lipophilic dye, 1,1'-dioctadecyl-3,3,3',3'-tetramethylindocarbocyanine perchlorate (DiI). DiI-labeled SKOV-3 exosomes were incubated with cells for 1 h before washing and cell imaging by CLSM (Figure 5). Prior to peptide binding, exosomes exhibited significant uptake in SKOV-3 cells, with punctate fluorescence patterning indicative of endocytic uptake (Figure 5c). Energy-dependent uptake of SKOV-3 exosomes by SKOV-3 cells has been previously reported.^[39] When scr-LXY30 (1×10^{-6} M) was preincubated with DiI-labeled SKOV-3 exosomes (and unbound peptide removed by centrifugal spin columns), we observed a significant ($p < 0.005$) decrease in uptake (Figure 5d). Preincubation with LXY30 at the same concentration significantly reduced uptake even compared to the scr-LXY30 case ($p < 0.005$) (Figure 5e). Increasing LXY30 concentration continued reducing uptake until 10×10^{-6} M, at which point further increase of concentration did not continue to increase prohibition of exosome uptake (Figure 5f). Furthermore, at incubation concentrations above 10×10^{-6} M, significant cell toxicity occurred. CLSM images were quantified by pixel intensity and normalized by cell area for statistical comparison (Figure 5a).

2.5. Capture of SKOV-3 EVs by Surface Immobilized LXY30

To assess the potential of immobilized LXY30 as a tumor-associated exosome capturing or detection agent, we applied multiparametric surface plasmon resonance (MP-SPR). While SPR has been recently applied to EV characterization, these reports were performed using surface-immobilized antibodies targeted against surface proteins of vesicles, for instance, anti-CD9 or anti-CD63.^[40] Since most types of EVs express such generic membrane proteins in their membrane surfaces, they are unable to distinguish between tumor and healthy EVs. Instead, in this proof-of-concept model system, we demonstrate that immobilized LXY30 peptide on an SPR chip surface could

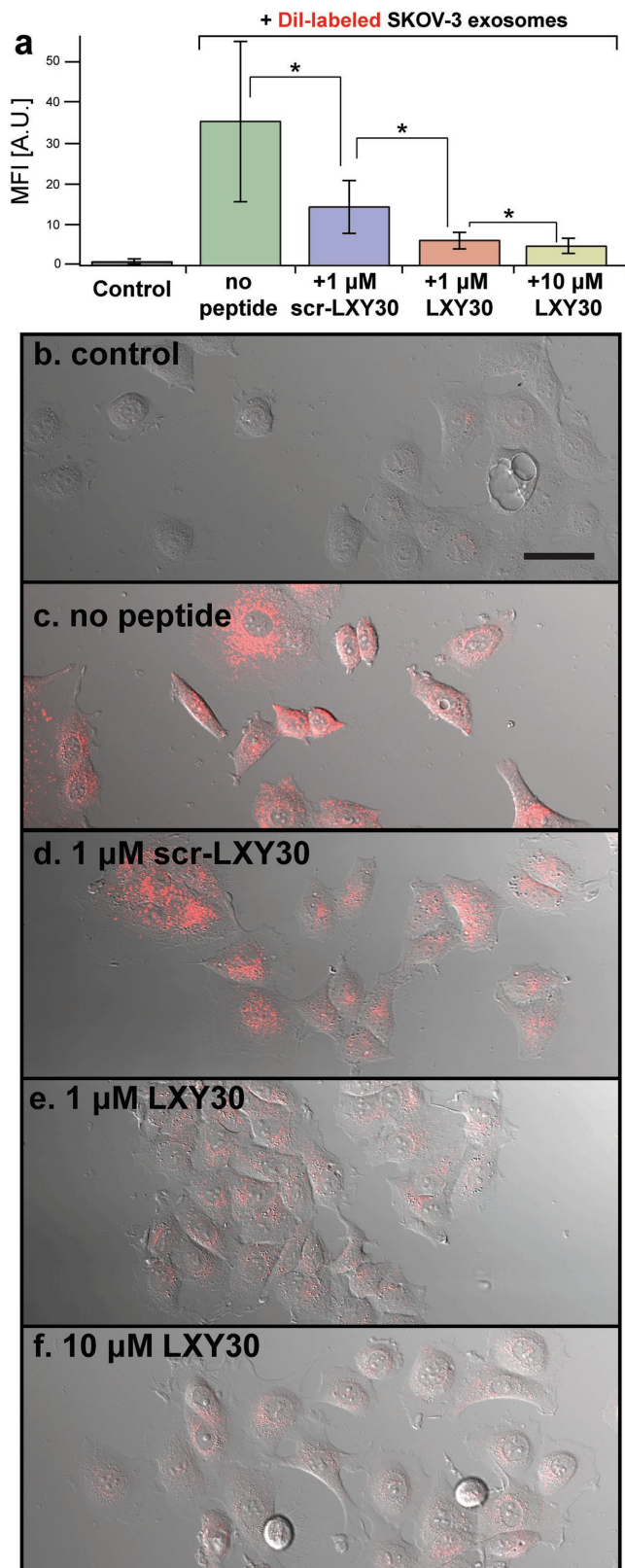


Figure 5. Effect of LX Y30-binding on cell uptake. a) Quantification of exosome uptake between conditions by measuring the mean fluorescence intensity (MFI) per SKOV-3 cell in representative CLSM images. b) CLSM control image of SKOV-3 cells with no Dil-labeled exosomes added. The

capture the tumor EVs, and furthermore, that the surface-associated bilayer of captured EVs can be characterized for average thickness (d) and refractive index (n). Moreover, by comparing the recorded shifts in the position of SPR peak minimum reflectance (Θ_{SPR}), interaction kinetics for peptide–EV binding can be calculated, including association/dissociation rate constants (k_a/k_d) and total binding affinity (K_D).

Figure 6 illustrates the MP-SPR scheme and relevant sensorgrams following EV injection. Several solutions are sequentially introduced by flowing over chips pre-coated with a self-assembled monolayer (SAM) of biotinylated-alkanethiol (11-mercapto-1-undecanol, MuOH). The MP-SPR instrument used here features two independent channels for parallel chip functionalization. To both channels, streptavidin was flown over and bound to the biotinylated surface, as confirmed by SPR response (Figure 6b). To flow channel 1 (Figure 6b, black), LX Y30-biotin was added (in increasing concentration to ensure complete surface coverage), while control flow channel 2 (Figure 6b, red) was not exposed to LX Y30-biotin. The subsequent injection of SKOV-3 exosomes in both channels at 100 min resulted in characteristic adsorption in the case of LX Y30-decorated surface (flow channel 1) but little to no exosome binding for the control without LX Y30-biotin (flow channel 2).

To assist modeling the kinetic parameters of binding, exosomes were serially injected at three different concentrations, representing 50 \times , 30 \times , and 10 \times dilutions (3.4×10^9 , 5.7×10^9 , and 1.7×10^{10} particles mL^{-1} , respectively). The sequential injections produced a stepwise signal reflecting the steady-state binding of exosomes at the sensor surface, corresponding to the three peaks evident in the flow channel 1 (Figure 6b outlined boxes, and examined more in detail in **Figure 7a**). For modeling the interaction kinetics, we employed a two-site binding model (the relevance of this model is discussed in the following section) allowing for two instances of LX Y30 ligand binding to a single vesicle. For three hypothetical cases where the integrin content at the exosome surface represents either (i) 1%, (ii) 5%, or (iii) 10% of the total protein per particle, the $\alpha_3\beta_1$ integrin concentration can be estimated. Hence, using the total protein ($0.65 \mu\text{g } \mu\text{L}^{-1}$) concentration, the initial particle concentration determined with the NTA (1.7×10^{14} particles L^{-1}), and the average molecular mass for a single $\alpha_3\beta_1$ complex (220 kDa), we estimated the $\alpha_3\beta_1$ integrin concentrations as listed in **Table 1**. These values were used to fit the model to the data for the three injected concentrations. The resulting interaction kinetics evaluation yielded two association rate constants, k_{a1} and k_{a2} , two dissociation rate constants k_{d1} and k_{d2} , and two binding affinities, K_{D1} and K_{D2} , respectively, for the possible cases (i), (ii), and (iii), as represented in **Table 2**. The results for binding affinities, K_{D1} varied in the range of $12\text{--}26 \times 10^{-9}$ M, and K_{D2} between 55 and 480×10^{-12} M, suggest strong binding of SKOV-3 exosomes to the surface-bound LX Y30 ligands. The low chi-squared values indicate that the data fitting was accurate. This can also be observed in **Figure 7a** displaying the measured (solid black

remaining images represent the conditions where Dil-labeled exosomes were added to cells after premixing with c) no peptide, d) 1×10^{-6} M scr-LX Y30, e) 1×10^{-6} M LX Y30, and f) 10×10^{-6} M LX Y30. The scale bar is 20 μm . * represents $p < 0.005$.

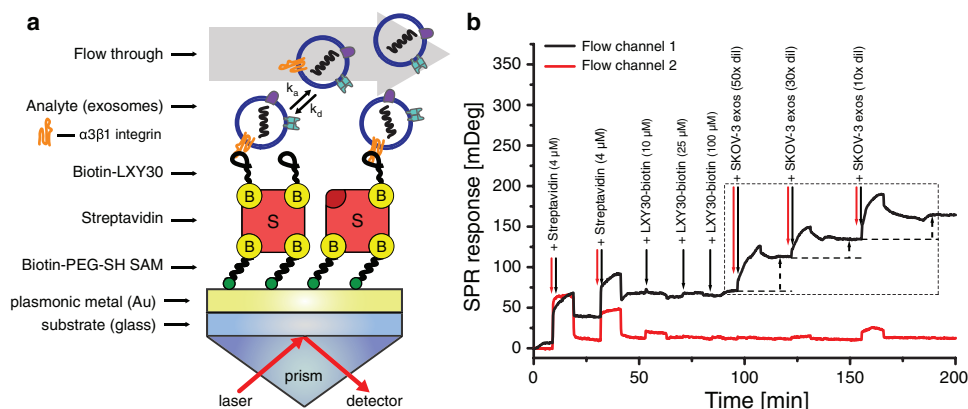


Figure 6. On-chip capture of tumor EVs. a) MP-SPR detection platform for tumor SKOV-3 exosomes using the surface-immobilized LXY30 capturing peptide. Each step of the peptide immobilization via streptavidin-biotin conjugation can be followed by SPR response. b) Sensorgram of the SKOV-3 exosome detection following biotin-PEG-SH self-assembled monolayer (SAM) formation. First, streptavidin was injected to both flow channels, followed by injections of LXY30-biotin in flow cell 1 only. Finally, SKOV-3 exosomes were injected to both flow channels. The characteristic adsorption outlined by the dotted box was modeled for extraction of kinetic parameters (Figure 7).

line) and calculated data (dotted lines) converging relatively well, and, furthermore, the calculated data appear independent of our assumption for protein coverage (1%, 5%, 10%).

The full angular SPR spectra (between 40° and 78°) before and after exosome adsorption (Figure 7b) was used to model adsorbed thickness (d) and refractive index (n) of the bilayer formed by the surface-bound SKOV-3 exosomes (displayed in Table 2). The layer modeling is based on the two-wavelength method,^[41,42] but for clarity Figure 7b displays only the 670 nm laser data and the last phase of layer modeling is illustrated, that is, the intermediate steps of layer modeling are omitted. The SPR peak minimum position undergoes an evident change from smaller angular values toward larger as the streptavidin and subsequent concentration series of SKOV-3 exosomes are associating to the surface. The refractive index of the resulting exosome layer was modeled at $n = 1.341$, slightly higher than

the approximate refractive index of an aqueous buffer solution, $n = 1.334$. This was expected given the presence of light refracting compounds such as proteins, lipids, and nucleic acids in the exosomes. The mass of bound SKOV-3 exosomes per sensor surface unit area (ng cm^{-2}) and the average height of the resulting exosome layer can also be estimated, based on calculation of surface mass density (Γ) increase yielded by the binding exosomes. First, the de Feijter equation and refractive index increment $dn/dc = 0.182 \text{ cm}^3 \text{ g}^{-1}$ are used to determine the dependency between the observed change in SPR peak minimum shift and the amount of mass adsorbed on the surface.^[43] For the employed SPR system, we obtain a conversion factor: $\Delta 1 \text{ mdeg} = \Delta(\Gamma) \approx 0.6 \text{ ng cm}^{-2}$. Thus, an estimate of $\approx 90 \text{ ng cm}^{-2}$ was calculated for surface mass density increase, with an average layer thickness of 34 nm, despite the size distribution of SKOV-3 exosomes to be measured by NTA at $177 \pm 5.4 \text{ nm}$. Possible explanations for this observation

are proposed in the following section.

3. Discussion

Of the $\alpha_3\beta_1$ integrin-expressing tumor cell lines found to bind LXY30 in preliminary studies, SKOV-3 ovarian tumor cells reliably produced the largest number of EVs with minimal effort in cell maintenance, and thus were chosen as the model cell line for this study. Jurkat human T lymphoid tumor cells were cultured as a control to measure integrin specificity, since they express $\alpha_4\beta_1$ and not $\alpha_3\beta_1$. Using western blot on SKOV-3 cell and SKOV-3 exosome lysates, we measured

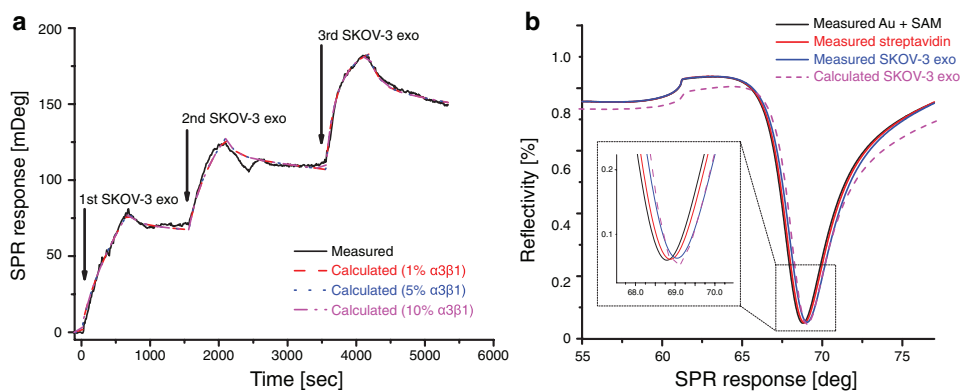


Figure 7. Kinetic modeling of MP-SPR sensorgrams. a) The solid black line shows the measured data during the three injections while the red, blue, and pink dashed lines depict the fitted data for the hypothesized cases of (i) 1%, (ii) 5%, and (iii) 10% coverage of $\alpha_3\beta_1$ integrin on the surface of a SKOV-3 exosome. b) Full SPR angular spectra recorded at various time points during the experiments; the black line represents the initial situation whereby the gold sensor surface and SAM layer were measured; the red line illustrates the events after the streptavidin injection and the following baseline stabilization; and the blue line is a snapshot after all three SKOV-3 concentrations were injected and a stable baseline was observed. The pink dashed line depicts the modeled fitting at the last phase of the interactions, that is, following the three SKOV-3 injections.

Table 1. Estimated $\alpha_3\beta_1$ integrin concentrations ($\times 10^{-9}$ M).

Exosome dilution	50×	30×	10×
1% coverage	0.62	1.03	3.09
5% coverage	3.09	5.15	15.5
10% coverage	6.20	10.3	30.9

the presence of both α_3 and β_1 integrins (Figure 1a), paving the way for targeting tumor-associated exosomes by (i) reproducing previous findings that tumor cells pass certain overexpressed integrins to their released exosomes,^[9] and (ii) identifying a target for LXY30 binding. Interestingly, α_3 was not readily detectable in the SKOV-3 cell lysate compared to the SKOV-3 exosome lysate, likely because it represents only a minor fractional component of the total loaded protein, yet we do demonstrate the presence of the α_3 subunit on SKOV-3 cells via significant anti- α_3 antibody binding to SKOV-3 cells when examined by flow cytometry (Figure 2c).

Flow cytometry is an increasingly important tool for EV characterization.^[44] Presently, exosomes themselves are too small to be easily and reliably examined by most flow cytometers, but they can be bound to 4 μm aldehyde/sulfate-coated latex beads for analysis (Figure 2b). The aldehyde functional groups can be covalently linked to lysine side chains on exosomal protein while the anionic sulfate groups confer colloidal stability to the beads during exosome binding. With this technique, we found that both $\alpha_3\beta_1$ -expressing SKOV-3 tumor cells and their released exosomes bind strongly to LXY30-Fl. When incubated with scr-LXY30-Fl, SKOV-3 cells exhibited a drastic reduction in binding, while their exosomes retained some nonspecific binding. Yet, SKOV-3 exosomes did not measurably bind anti- α_3 antibody, nor did prior incubation with anti- α_3 inhibit LXY30 binding. This finding could be interpreted by considering the state of the integrin membrane protein under extreme membrane curvature, as is the case for nanoscale vesicles. At this scale, a biomembrane's extreme geometrical curvature can critically influence biochemical properties, with some reports suggesting occurrence of significant protein conformational changes.^[45] We hypothesize that this may result in poor antibody affinity for exosomal integrins, despite high affinity toward cell membrane integrins. This point will be investigated further in future studies, but is a good example of an advantage of peptide binding in place of immunoaffinity methods.

Following bulk flow cytometry measurement of LXY30-EV binding, we applied our recently reported technique of LTRS. A complete discussion of the application of LTRS to optically trap and subsequently measure the chemical composition of

EVs can be found in our recent publication.^[38] While a major advantage of Raman spectroscopy is label-free characterization, we strengthened the technique with the addition of Raman tags, extending the capability of LTRS to measuring ligand binding on a single exosome. As illustrated in Figure 4b, ligand binding can be quantified in a particular region where spontaneous Raman scattering peaks arise from either the LXY30-RT (Peak A, alkyne, 1600 cm^{-1}) or exosomes (Peak B, a grouping of 1651 cm^{-1} from C=C stretching, and 1668 cm^{-1} from amide I vibrations). The table in Figure 4b lists the spectra by descending vesicle peak height (Peak B), and it is evident that the ratio of Peak A to Peak B fluctuates randomly. In other words, for a given single vesicle (i.e., a single trace in Figure 4a), the peaks did not scale together, as might be expected if one assumes that Peak B represents relative exosome amount (protein/lipid content) and that integrin number scales with vesicle size. This may represent a varied expression in integrin distribution across subpopulations of vesicles that may not scale with vesicle surface area, or instead, variation in LXY30-integrin binding. Although we could not extract binding stoichiometry in this case, we regard Raman tagging of small molecules as a major innovation for examining binding to single extracellular vesicles.

Interestingly, LXY30 binding was able to inhibit cell uptake of the SKOV-3 exosomes by their parent cells. By premixing DiI-labeled SKOV-3 EVs with LXY30, we observed a reduction in cell uptake up to $\approx 80\%$. Preincubation with scr-LXY30 reduced uptake by $\approx 50\%$, corroborating our flow cytometry results that some weak binding of scr-LXY30 still occurs, though significantly reduced ($p < 0.005$) compared to LXY30. Some fluorescence was still observed even at saturation of LXY30 (i.e., higher amount of LXY30 did not further decrease uptake), indicating that even by blocking the $\alpha_3\beta_1$ -mediated uptake, some other independent mechanisms remain intact. The mechanisms by which integrin blocking reduces cell uptake are unclear, but given that circulating tumor exosomes are heavily implicated in tumorigenesis, this observation renders LXY30 useful for potential therapeutic application, and will be a topic of future investigation in our lab.

Several recent studies and reviews have reported on the feasibility of applying extracellular vesicles to therapeutic or diagnostic application, emphasizing the importance of developing EV marker assays that outperform and/or complement conventional diagnostics.^[46–48] In that context, the flow cytometry and LTRS methodologies presented above would be challenging to adopt in clinical settings. In fact, most traditional exosome characterization assays typically rely on various techniques requiring labels that alter the biochemical structures of interest, or are limited to sampling rate, thus not offering information

Table 2. The results of interaction kinetics analysis, bilayer characterization, and surface mass density calculations.

Estimated $\alpha_3\beta_1$	k_{s1} [$\text{M}^{-1}\text{ s}^{-1}$]	k_{d1} [s^{-1}]	K_{D1} [M]	k_{s1} [$\text{M}^{-1}\text{ s}^{-1}$]	k_{d2} [s^{-1}]	K_{D2} [M]	χ^2
(i) 1%	$5.14 \times 10^5 \pm 6.97 \times 10^3$	$9.35 \times 10^{-3} \pm 9.11 \times 10^{-5}$	$1.82 \times 10^{-8} \pm 4.23 \times 10^{-10}$	$1.28 \times 10^6 \pm 7.28 \times 10^2$	$7.00 \times 10^{-5} \pm 1.88 \times 10^{-5}$	$5.46 \times 10^{-11} \pm 1.47 \times 10^{-11}$	7.52
(ii) 5%	$6.32 \times 10^5 \pm 1.85 \times 10^4$	$7.30 \times 10^{-3} \pm 1.54 \times 10^{-4}$	$1.16 \times 10^{-8} \pm 5.83 \times 10^{-10}$	$2.52 \times 10^5 \pm 5.93 \times 10^2$	$6.05 \times 10^{-5} \pm 2.53 \times 10^{-5}$	$2.40 \times 10^{-10} \pm 1.01 \times 10^{-10}$	6.46
(iii) 10%	$2.90 \times 10^5 \pm 1.86 \times 10^4$	$7.40 \times 10^{-3} \pm 1.26 \times 10^{-4}$	$2.55 \times 10^{-8} \pm 2.08 \times 10^{-9}$	$1.26 \times 10^5 \pm 6.30 \times 10^2$	$6.07 \times 10^{-5} \pm 2.13 \times 10^{-5}$	$4.82 \times 10^{-10} \pm 1.71 \times 10^{-10}$	6.47
d [nm]	n	Surface mass density increase [ng cm^{-2}]					
34	1.341	$\Delta(\Gamma) = 90$					

in real time. One recent review by Lener et al. extensively describes the requirements for EV-based therapeutics, outlining the challenges in costs, reproducibility, effectiveness, throughput, and limit of detection.^[48] For those reasons, we applied the technique of MP-SPR to measure LXY30 binding. MP-SPR is extremely sensitive label-free optical measurement method based on detecting plasmonic phenomena enhanced by a nearby metal surface. MP-SPR measurements can be made in real time, allowing for constant monitoring of interaction events. It also employs a microfluidic flow system enabling measurements under steady state or dynamic flow conditions, and thus is considered more relevant for characterizing physicochemical phenomena in biological environments. Furthermore, at their best, plasmonic-based measurements offer at least an order of magnitude in increased detection sensitivity compared to ELISA or fluorescence-based detection methods,^[49] therefore it will be an excellent direction to explore in future studies examining binding to clinical samples.

Using MP-SPR, we confirmed the ability for SKOV-3 exosomes to bind to LXY30 modified surfaces. We adopted the commonly used one-to-two (1:2) binding model for analyte adsorption, taken from previous observations that the CD63 tetraspanin proteins on exosomal membranes exhibit such binding behavior.^[14] From a physical standpoint there may be more than two binding sites per exosome, but it has been observed that the two strongest sites are dominant, and other binding events are typically undetected.^[50] It is noteworthy that the 1:2 binding model is also applicable to binding schemes where heterogeneous immobilization of the target (i.e., LXY30) at the surface may have occurred. We expect that this is likely the case in our measurements, since the modeling resulted in good data fitting as seen by visual inspection in Figure 7. The calculated interaction kinetics parameters (Table 2) did not show strong dependency on the estimated amount of $\alpha_3\beta_1$ integrin proteins on the membranes of SKOV-3 exosomes. This observation may suggest that the binding of SKOV-3 exosomes occurs as long as there are at least some $\alpha_3\beta_1$ found on the surfaces of exosomes available for binding. The results of the layer modeling also suggest that either (i) significant vesicular shape deformation events may occur during the exosome binding or at the surface after binding, (ii) surface-bound LXY30 captures exosomes of certain diameter or up to some maximum diameter, or more likely that (iii) the coverage of exosomes at the surface is uneven. The latter is a technical limitation of optical modeling, as mathematical fitting of the measured angular SPR spectra to the models by Fresnel's equations is made by averaging over the laser spot area on the gold sensor surface, $\approx 1 \text{ mm}^2$ in diameter. Therefore, empty spaces in the surface-bound layer under the laser spot would result in underestimating the calculated layer thickness and refractive index. In recent SPR-vesicle literature, physical models have been developed to correlate change of refractive index with exosome concentration.^[51,52] In those models, both particle shape deformation and surface unevenness (due to wide particle size distribution) were considered. The bilayer thickness modeling in this study strengthens those previous observations, namely, that shape deformation may play a role in exosome interactions and should be taken into account.

While the layer modeling yielded rational results with satisfactory accuracy within the context of this study, and had resemblance to other recent investigations,^[52] intriguing questions merit further studies. For example, we plan to examine the differences between interaction kinetics and bilayer compositions for exosomes from different cell types. A prerequisite for such studies is that additional exosome-specific capturing ligands are found and synthesized, currently underway. Finally, calculation of the limit of detection (LOD) also warrants subsequent assays in order to find out the feasibility of this platform for early-stage cancer detection by sensing tumor-associated exosomes in human biofluids.

4. Conclusions

EVs isolated from various biological fluids are essentially a mixture of distinct types of vesicles that have originated from various parent cells. Hence, the capability to detect certain types of EVs, such as tumor-associated ones, is essential for their exploitation as diagnostic agents. Since integrins are known to be highly overexpressed on cancer cells, and are trafficked to those cells' released EVs, we developed a methodology for characterizing the specific targeting of integrin-binding peptides to cancer cell released EVs. Our in-house peptide, LXY30, selectively binds the $\alpha_3\beta_1$ integrin overexpressed on cells comprising many types of epithelial cancers, including ovarian adenocarcinoma cells. In SKOV-3 ovarian tumor cell released EVs (that were determined to be primarily exosome-type), protein quantification revealed the presence of both α_3 and β_1 integrin subunits. On-bead flow cytometry was used to characterize ensemble LXY30 peptide binding to SKOV-3 exosomes, but not other types of Jurkat-tumor-cell-derived exosomes. Laser tweezers Raman spectroscopy confirmed that LXY30 peptide binding occurs at the single vesicle level. Furthermore, by confocal microscopy, we determined that LXY30 could dramatically reduce SKOV-3 exosome uptake by their parent cells. Finally, we present a convenient and straightforward method to capture and detect cancerous SKOV-3 exosomes in real time by MP-SPR, without a priori labeling. This platform allowed for monitoring the interaction kinetics of and bilayer properties of SKOV-3 vesicles with the surface-immobilized LXY30 capturing ligand. The characterization schemes outlined here, along with the first report of a ligand capable of discriminating tumor and nontumor EVs, represent major steps in improving the potential of EVs for nanomedical-based therapeutic and diagnostic systems.

5. Experimental Section

Unless otherwise noted, all reagents and materials were purchased from Sigma-Aldrich Corp. (St. Louis, MO) and used without further purification. Cell lines were purchased from ATCC (Manassas, VA).

Cell Culture: Human ovarian carcinoma SKOV-3 cells were grown in McCoy's 5A media and human T-cell leukemia Jurkat cells were grown in RPMI 1640 medium. Each medium was supplemented with FBS (10%), penicillin (100 units mL^{-1}), and streptomycin (100 $\mu\text{g mL}^{-1}$). Cells were subcultured (37 °C, 5% CO_2) and regularly maintained by splitting upon reaching an estimated 80% confluence. Contaminating EVs are found

in high concentration in FBS and must be removed before exosome collection. In vitro serum-free conditions have been demonstrated to increase oxidative stress, leading to generation of unintended EV release,^[53] therefore it is preferred to deplete FBS of exosomes by ultracentrifugation. Typically, 30% FBS (150 mL) in appropriate culture medium was loaded in the rotor-type 50.2 Ti (Beckman Coulter, polycarbonate bottles, prod. no. 355618) and spun at 100 000×g, 4 °C, >18 h. After centrifugation, supernatants were filtered (0.2 μm) and diluted with appropriate medium to 10% FBS. Clearing of bovine EVs is regularly confirmed by NTA. It was observed that exosome yield began to drop significantly if a cell line was grown in prolonged absence of EV-depleted FBS, therefore cells past five generations after thawing from liquid nitrogen were not cultured.

Ultracentrifugation Isolation: After 48–72 h of incubation with EV-depleted medium, cell culture supernatant was decanted and subjected to low-speed centrifugation to clear any cells (300×g, 5 min, 4 °C), dead cells (2000×g, 10 min, 4 °C), and cell debris (10 000×g, 30 min, 4 °C). The resulting supernatant was centrifuged twice at 100 000×g, 4 °C, 2 h (rotor type: SW 28 Ti, tubes: thickwall polypropylene), dissolving and diluting the pellet in PBS between spins to remove contaminating free protein. For every 20 million cells at the time of EV harvest, the final exosome-containing pellet was dissolved in sterile DPBS (25 μL). Aliquots were stored at –80 °C for up to one month. Human plasma was obtained from healthy volunteers and deidentified via the UC Davis biorepository for laboratory use. Plasma obtained from three different patients (≈0.5–1.0 mL each) was used as controls in this study. Whole plasma was subjected to identical ultracentrifugation isolation as described above for cell culture supernatant.

Western Blot: All reagents listed by part number in this section were purchased from ThermoFisher Scientific. Following exosome lysis with RIPA buffer (prod. no. 89900), protein concentration was measured by BCA assay (Pierce kit, prod. no. 23225) according to manufacturer's instructions. For WB analysis, exosome aliquots containing 20 μg protein (as determined by BCA assay) were lysed in SDS sample buffer: 2% (w/v) sodium dodecyl sulfate, 125 × 10⁻³ M Tris-HCl at pH 6.8, 12% (v/v) glycerol, 0.05% (w/v) bromophenol blue, and DTT (50 × 10⁻³ M). For proteins that should not be reduced prior to immunostaining (tetraspanins CD9 and CD63), DTT was omitted and its volume replaced by PBS. To obtain cell lysates, cell suspensions were washed by repeated (3×) pelleting (300×g, 5 min) and dissolution in sterile DPBS. After three washes, the cell pellet was dissolved in RIPA lysis buffer with protease inhibitor (prod. no. 78420), and briefly vortexed before and after 30 min incubation on ice. Following incubation the solution was centrifuged to precipitate insoluble membrane components and other impurities (18 000×g, 30 min, 4 °C) and resulting supernatant frozen for up to six months at –80 °C. Protein aliquots (20 μg) were dissolved in Laemmli sample buffer (prod. no. NP0008), supplemented appropriately with reducing agent, just prior to gel loading. After dissolution in appropriate loading or lysis buffer, EV and cell lysates were incubated at (95 °C, 5 min) while shaken (900 rpm) and then centrifuged (1 min, 13 000×g).

Gel electrophoresis of lysed EVs or cell was performed by first loading samples (20 μg protein/well) onto 4%–12% Bis-Tris ten-well precast gels (NuPage Novex, prod. no. NP0335) and filling the electrophoresis rig (Xcell Surelock gel tank) with MOPS buffer (Nu-Page, prod. no. NP000102). Proteins were separated at 90 V for 30 min, then 120 V until complete. The gel was carefully removed, washed with buffer, and transferred to nitrocellulose membrane (prod. no. 88018) for 2 h at constant current of 400 mA, with the entire WB module submerged in ice. The resulting blots were removed and blocked overnight by submerging in blocking buffer: 5% (w/v) nonfat dairy milk in Tris-buffered saline with Tween (TBST) buffer. For immunostaining, primary antibody was appropriately diluted in blocking buffer according to its datasheet and incubated with blot for 1 h at room temperature while gently shaking. The following primary antibodies were used: mouse monoclonal anti-CD63 (ThermoFisher Scientific), mouse monoclonal anti-CD9 (ThermoFisher Scientific), rabbit polyclonal anti-tsg101 (Sigma Aldrich, St. Louis, MO), rabbit polyclonal anti-calnexin (Cell

Signaling Technology, Danvers, MA), and mouse monoclonal anti-α₃ and anti-β₁ integrins (Santa Cruz Biotechnology, Dallas, TX). The blots were washed (3× TBST, 5 min) and incubated with HRP-conjugated secondary antibody diluted in blocking buffer (1:2000) for 1 h. Secondary antibodies were goat antirabbit and goat antimouse immunoglobulin (Santa Cruz Biotechnology, Dallas, TX). ECL substrate (prod. no. 35050) was used to develop blots according to manufacturer's instructions and immunoactive bands detected by chemical imaging (Bio-Rad ChemiDoc Hercules, CA). Representative WB for SKOV-3 cell lysate and exosomes is shown in Figure 1a.

Electron Microscopy: EVs were contrasted and embedded for whole-mount EM analysis according to previously reported methods.^[35] Briefly, fresh EV-containing UC pellets were directly resuspended in 2% (w/v) paraformaldehyde in PBS, with 5 μL deposited on Formvar carbon-coated EM grids. The grids were sequentially floated on several 20–50 μL drops for washing (PBS), fixing (glutaraldehyde), contrasting (uranyl oxalate), and further contrasting/embedding (uranyl acetate/methyl cellulose). Grids were subsequently imaged by EM at 80 kV (Philips CM120). A representative EM image of SKOV-3 derived EVs is displayed in Figure 1b.

Atomic Force Microscopy: An aliquot (50 μL) of diluted (1:200) purified SKOV-3 EVs was pipetted onto a freshly cleaved mica sheet and air dried. Images were acquired with an Oxford-Asylum Research MFP-3D AFM and K-TEK Nanotechnologies Tetra14 silicon lever with a spring constant of about 5. Pixel resolution was 512 × 512 and scan rate was 0.5 Hz. Topography and Z-sensor images were flattened using mean surface data to establish a reference plane. Amplitude images were also taken in order to show edge enhancements, approximating the EV surface gradient. A representative AFM amplitude image for SKOV-3 EVs is shown in Figure 1c.

Nanoparticle Tracking Analysis: NTA was recorded on a NanoSight LM10 instrument with illumination at 488 nm. Following dilution of purified EVs (1:1000) in triple-filtered PBS, samples were introduced by perfusion pump. For a typical experiment, three 60 s videos were recorded, with 30 s of sample flow between replicates. Concentration was confirmed to be in the acceptable range for NTA analysis (3–20 × 10⁸ particles mL⁻¹), or else diluted/concentrated appropriately and reanalyzed.

Peptide Synthesis: Solid-phase peptide synthesis was used to synthesize LXY30 and scr-LXY30 peptides. Rink amide resin (0.52 mmol g⁻¹ loading) was chosen as the solid support in order to facilitate peptide synthesis and eventual cleavage from the resin. HPLC (high-performance liquid chromatography) grade dimethylformamide (DMF) was used for coupling and analytical reagent grade DMF, dichloromethane (DCM), and methanol (MeOH) were used for washing of the resin throughout synthesis. Resin was swollen overnight in DMF in a polypropylene column with frit and tight-sealing cap, enabling easy washing via bead retention between coupling steps. The protecting Fmoc group was removed from the resin by 20% (v/v) 4-methyl piperidine/DMF solution (2 × 15 min), and the resin was washed by DMF (15 mL × 3), MeOH (15 mL × 3), and DCM (15 mL × 3). Standard Fmoc/*t*-But peptide chemistry was used to couple the amino acids to the resin. For each coupling step, 5 molar eq. of COMU ((1-cyano-2-ethoxy-2-oxoethylideneaminoxy) dimethylamino-morpholino-carbenium hexafluorophosphate) and 10 molar eq. DIEA (*N,N*-diisopropylethylamine) were added with 5 molar eq. of Fmoc-protected amino acid. After 1 h of light agitation, Kaiser test was used to confirm complete reaction. Following coupling, the Fmoc group was again removed by 4-methyl piperidine/DMF solution, confirmed by Kaiser test. Prior to cleavage from the bead, the disulfide in the peptide was formed. Iodine (8 molar eq. to resin, dissolved in DCM) was used to simultaneously deprotect trityl chemical groups on the cysteine residues and oxidize the thiols to form a ring. The resin was subsequently washed with copious DMF and aqueous ascorbic acid to quench and remove excess iodine. Finally, the resin was mixed for 3 h with slight agitation at room temperature with a cleavage cocktail (82.5% trifluoroacetic acid, 5% thioanisole, 5% water, 5% phenol, and 2.5% triisopropylsilane, all % are v/v), resulting in both removal of side chain protecting groups and cleavage from the resin. The peptide-containing

filtrate was collected and concentrated under a gentle stream of air for 30 min. A large volume of cold diethyl ether was added to precipitate the crude peptide, which was collected after brief centrifugation (3000×g, 5 min), washed again with diethyl ether, and dissolved in water for HPLC purification. 5×10^{-3} M peptide stock solutions were stored at 4 °C until needed. For flow cytometry detection, peptide analogues were additionally conjugated at their N-terminus with a short PEG spacer (N-[8-(9-fluorenylmethyloxycarbonyl)amino-3,6-dioxaoctyl]succinamic acid, Ebes) and FITC dye. For both reactions, 4 molar eq. plus 8 eq. DIEA were mixed with beads in DMF for 2 h before washing. Reaction steps were confirmed by Kaiser test. For LTRS measurement, 4-(phenylbuta-1,3-dien-1-yl)benzoic acid (RT) was covalently conjugated to the peptide N-terminus via PEG spacer (Figure S1, Supporting Information) under similar coupling conditions. Peptide molecular weight was confirmed by matrix-assisted laser desorption/ionization time-of-flight (MALDI TOF) mass spectrometry (Bruker UltraFlex™). Figure S1 (Supporting Information) displays a representative mass spectrum for purified LXY30-RT peptide.

Flow Cytometry: For whole cell flow cytometry, cells were trypsinized (if necessary) and aliquoted in 3% (v/v) FBS in PBS with LXY30-FI or scr-LXY30-FI peptide (to 1×10^{-6} M). For integrin binding, 1 µg mouse monoclonal anti- α_3 -FI (200 µg mol⁻¹, Santa Cruz Biotechnology, Dallas, TX) was added per million cells. After 30 min incubation, cells were washed thrice and finally resuspended with 3% FBS and 1% sodium azide.

On-bead flow cytometry of antibody–exosome binding was performed according to previous reported methods,^[35] by passive adsorption to 3.9 µm latex beads with aldehyde/sulfate groups grafted to the polymer surface (ThermoFisher Scientific, prod. no. A37304). Only one change to the protocol was made for peptide incubation: exosomes were labeled with peptide prior to bead adsorption. Briefly, exosomes (10 µg in 15 µL, as measured by BCA assay) were mixed overnight with LXY30-FI or scr-LXY30-FI (1 µL, 5×10^{-3} M). Labeled exosomes were purified from free peptide by centrifugal spin column (ThermoFisher Scientific, MWCO: 3000 Da, prod. no. 4484449) according to manufacturer's instructions.

Prepared whole cells or exosome-coated latex beads were promptly analyzed by flow cytometry (Becton Dickinson Fortessa). Three side-by-side replicates were performed for each condition and at least 10 000 gated cells or beads were analyzed for each replicate. Typical gating strategies for SKOV-3 cells and latex beads are displayed in Figure S2 (Supporting Information).

Laser Tweezers Raman Spectroscopy: Raman measurements were made on a purpose-built LTRS system that was described previously.^[38] Briefly, 785 nm laser light (CrystalLaser, Reno, NV) was coupled into a 60×, 1.2 NA water immersion objective on an inverted microscope platform (Olympus IX-71). 25 mW of light reaches a diffraction limited spot with a spot size of about 1 µm. This is capable of trapping single exosomes and other nanoparticles, as well as larger clusters of particles. Raman scattered light is generated by the same laser, and this Stokes-shifted light is collected back through the objective. It is separated from the primary beam through a dichroic beam splitter and edge filter (both Chroma Technology, Bellows Falls, VT). The Raman signal was then coupled into a multimode optical fiber and launched into a spectrograph (SpectraPro 2300i, Princeton Instruments, Trenton, NJ) and dispersed on a CCD (Pixis 100, Princeton Instruments).

In the experiments, five 60 s spectral frames were recorded, for a total of 300 s integration time, and then imported into MATLAB for data processing using home-brewed scripts. For the data pretreatment, all spectra were corrected for cosmic rays using a median threshold filter described previously by Beier.^[54] By comparing spectra pixelwise across the five frames, outlier values caused by cosmic rays can be easily detected and their value replaced by the framewise median. The cosmic-ray-corrected frame-level spectra were averaged to produce a single, 300 s integration time spectrum for each sample. The spectra were then smoothed using the Whittaker smoother proposed by Eilers^[55] with a Lagrange parameter of 5. After smoothing, asymmetric least squares (AsLS) to fit a background to the data were used. The background is composed of quartz, PBS buffer, and a fifth-order polynomial

representing autofluorescence in the system. For the AsLS modeling, an asymmetry parameter of $p = 0.001$ to heavily penalize negative residuals was used, allowing to obtain spectra free of any background contamination.^[38,56,57] Following background correction, all spectra were normalized to the area under the curve (vector normalization). Thus, the y-axis of the Raman spectra then represents the proportion of individual chemical groups relative to the total chemical content within the sampling volume. Instead, for comparison of absolute quantity of chemical content (Figure 4a), no normalization was performed.

For peptide labeling experiments, LXY30-RT or scr-LXY30 were added to the vesicles during imaging on the coverslip to a final concentration of 100×10^{-6} M. At this concentration in the absence of EVs, the notable peaks arising from the RT could not be discerned. To measure the Raman spectra for ligand alone, poorly soluble aggregates of LXY30-RT were trapped before full dissolution in water.

Exosome Uptake by Confocal Laser Scanning Microscopy: To label the membrane of EVs for cell uptake visualization, the lipophilic dye Dil (Life Technologies, Catalog No. D3911) was used. A stock solution (10×10^{-6} M) of Dil in MeOH was diluted 100-fold with SKOV-3 EVs (30 µg) to a final volume of 200 µL in PBS containing 0.5% BSA.^[39] Dil-labeled EVs were diluted 50-fold with McCoy's media supplemented with 10% EV-cleared FBS and pelleted at 100 000×g, 4 °C, 2 h. The pellet was resuspended in McCoy's media. Aliquots (5 µg) Dil-labeled SKOV-3 EVs were mixed with either LXY30 or scr-LXY30 to final concentrations of 1 or 10×10^{-6} M. For blank controls, the peptide solution was replaced by PBS. After overnight incubation at 4 °C with gentle agitation, EVs were purified from unbound ligand by centrifugal spin column (ThermoFisher Scientific, MWCO: 3000 Da, prod. no. 4484449) according to manufacturer's instructions.

SKOV-3 cells were plated in an eight-well ibiTreat µ-slide chambers (ibidi USA, Inc.) at a starting concentration of 10 000 cells per well in serum-containing McCoy's media (300 µL). After 24 h, the cells were washed thrice with PBS and replaced with fresh media supplemented with 10% EV-cleared FBS. For each experimental replicate, Dil-labeled SKOV-3-EVs (1 µg) were added to each well. After 1 h, the cells were washed thrice with PBS, finally replaced in fresh PBS (200 µL), and promptly imaged under confocal microscopy with the appropriate filter set. Images were exported to ImageJ for analysis. The average fluorescence intensity and standard deviation (normalized by cell area) were measured and corrected by representative background areas. The statistical significance of differences in mean values was assessed using a two-sample independent Student's *t*-test at the 99.5% confidence level. Differences were reported using *P* values.

Multiparametric Surface Plasmon Resonance: The MP-SPR Navi 200 (BioNavis Ltd., Tampere, Finland) instrument was used for the surface plasmon resonance measurements. The system was equipped with two wavelength lasers, 670 and 785 nm, for plasmon excitation at the metal surface. In addition, it consisted of two independent microfluidic channels having inflow and outflow PEEK tubing, a controllable peristaltic pump for buffer flow, and a 12-port chromatography injector for the sample injections. Both of the channel surfaces were scanned with both incident wavelengths (i.e., 670 nm laser spot in flow channel 1 and flow channel 2; 785 nm laser spot, correspondingly) over a wide angular area of $\approx 40^\circ$ – 78° . Such a scanning method allows for recording full SPR angular spectra instead of the narrow angular window near the SPR peak minimum that is typically measured with traditional SPR instruments.

The sensor surface was designed as a biofunctional multilayered composition whereby the bottom molecular layer consisted of a SAM structure. The protocol for SAM establishment on a plain gold sensor surface was adopted from previous works describing the robustness and versatility of such molecular construction.^[58] In brief, the gold sensor was incubated overnight ex situ in a glass vial sealed with wax membrane in MuOH: biotin–PEG–thiol mixture in molar ratio 90%:10% in 88% EtOH. Immediately before using, the sensor was washed three times with excess amount of 99% EtOH and gently dried under nitrogen gas flow and mounted into the instrument. Consequently, in order to associate streptavidin to the biotin moieties of SAM, streptavidin solution

(4×10^{-6} M) was flown over the SAM surface in situ at constant flow speed ($20 \mu\text{L min}^{-1}$) in TRIS-EDTA (25×10^{-3} M TRIS, 1×10^{-3} M EDTA, pH 8.0) running buffer. Finally, after the streptavidin immobilization, using two independent microfluidic channels in the MP-SPR instrument, one channel surface was functionalized with biotinylated LXY30 peptide (LXY30-biotin) in constant TRIS-EDTA buffer flow ($15 \mu\text{L min}^{-1}$) onto the gold sensor slide, while the other channel remained without LXY30 and was exposed to only buffer flow. The interactions of three different concentrations of SKOV-3 exosomes with the surface-associated LXY30-biotin were carried out using a flow speed of $10 \mu\text{L min}^{-1}$. Evaluation of interaction kinetics was performed using TraceDrawer 1.6 software (Ridgeview Instruments AB, Vänge, Sweden). LayerSolver 1.2.1 software (BioNavis Ltd., Tampere, Finland) was used for the bilayer thickness and refractive index modeling.

Supporting Information

Supporting Information is available from the Wiley Online Library or from the author.

Acknowledgements

R.P.C. acknowledges support from the NIH T32 HL007013 training grant and the Ovarian Cancer Education and Research Network (OCERN) Research Grant. This work was also supported in part by NIH CA115483 awarded to K.S.L. T.R. acknowledges support from the Doctoral Programme in Materials Research and Nanosciences (MATRENA) and T.R., T.V., and M.Y. acknowledge support from the Finnish Funding Agency for Innovation (Funding No. 551/31/2015: "EV-Extra-Tox" project). The authors also acknowledge the US NSF Grant No. DBIO722538 for purchasing the NMR spectrometer. Ovarian cancer specimens were provided by the UC Davis Comprehensive Cancer Center Biorepository which was funded by the UC Davis Comprehensive Cancer Center Support Grant (CCSG) awarded by the National Cancer Institute (NCI). The authors are grateful to the following people for resources, discussions, and suggestions: Prof. Sebastian Wachsmann-Hogiu (UC Davis), Prof. James Chan (UC Davis), Dr. Alan Hicklin (UC Davis), Pat Kysar (UC Davis), and Prof. Zachary J. Smith (University of Science and Technology of China).

Conflict of Interest

The authors declare no conflict of interest.

Keywords

biosensors, cancer, diagnostics, exosomes, optical tweezers

Received: December 8, 2016

Revised: February 18, 2017

Published online: April 3, 2017

- [1] A. C. Society, *Cancer Facts and Figures*, Am. Chem. Soc. **2015**.
 [2] C. V. Harding, J. E. Heuser, P. D. Stahl, *J. Cell Biol.* **2013**, *200*, 367.
 [3] K. D. P. Dorayappan, J. J. Wallbillich, D. E. Cohn, K. Selvendiran, *Gynecol. Oncol.* **2016**, *142*, 199.
 [4] C. Gerçel-Taylor, S. Atay, R. H. Tullis, M. Kesimer, D. D. Taylor, *Anal. Biochem.* **2012**, *428*, 44.
 [5] J. C. Akers, V. Ramakrishnan, R. Kim, S. Phillips, V. Kaimal, Y. Mao, W. Hua, I. Yang, C. Fu, J. Nolan, I. Nakano, Y. Yang, M. Beaulieu, B. S. Carter, C. C. Chen, *J. Neurooncol.* **2015**, *123*, 205.
 [6] A. S. Azmi, B. Bao, F. H. Sarkar, *Cancer Metastasis Rev.* **2013**, *32*, 623.
 [7] C. Ciardiello, L. Cavallini, C. Spinelli, J. Yang, M. Reis-Sobreiro, P. de Candia, V. Minciocchi, D. Di Vizio, *Int. J. Mol. Sci.* **2016**, *17*, 175.
 [8] S. A. Melo, H. Sugimoto, J. T. O'Connell, N. Kato, A. Villanueva, A. Vidal, L. Qiu, E. Vitkin, L. T. Perelman, C. A. Melo, A. Lucci, C. Ivan, G. A. Calin, R. Kalluri, *Cancer Cell* **2014**, *26*, 707.
 [9] A. Hoshino, B. Costa-Silva, T.-L. Shen, G. Rodrigues, A. Hashimoto, M. T. Mark, H. Molina, S. Kohsaka, A. Di Giannatale, S. Ceder, S. Singh, C. Williams, N. Slop, K. Uryu, L. Pharmed, T. King, L. Bojmar, A. E. Davies, Y. Ararso, T. Zhang, H. Zhang, J. Hernandez, J. M. Weiss, V. D. Dumont-Cole, K. Kramer, L. H. Wexler, A. Narendran, G. K. Schwartz, J. H. Healey, P. Sandstrom, K. Jørgen Labori, E. H. Kure, P. M. Grandgenett, M. A. Hollingsworth, M. de Sousa, S. Kaur, M. Jain, K. Mallya, S. K. Batra, W. R. Jarnagin, M. S. Brady, O. Fodstad, V. Muller, K. Pantel, A. J. Minn, M. J. Bissell, B. A. Garcia, Y. Kang, V. K. Rajasekhar, C. M. Ghajar, I. Matei, H. Peinado, J. Bromberg, D. Lyden, *Nature* **2015**, *527*, 329.
 [10] D.-S. Choi, D.-K. Kim, Y.-K. Kim, Y. S. Gho, *Proteomics* **2013**, *13*, 1554.
 [11] T. Katsuda, N. Kosaka, T. Ochiya, *Proteomics* **2014**, *14*, 412.
 [12] H. Etayash, A. R. McGee, K. Kaur, T. Thundat, *Nanoscale* **2016**, *8*, 15137.
 [13] S. A. Melo, L. B. Luecke, C. Kahlert, A. F. Fernandez, S. T. Gammon, J. Kaye, V. S. LeBleu, E. A. Mittendorf, J. Weitz, N. Rahbari, C. Reissfelder, C. Pilarsky, M. F. Fraga, D. Piwnica-Worms, R. Kalluri, *Nature* **2015**, *523*, 177.
 [14] H. Im, H. Shao, Y. I. Park, V. M. Peterson, C. M. Castro, R. Weissleder, H. Lee, *Nat. Biotechnol.* **2014**, *32*, 490.
 [15] H. Ogata-Kawata, M. Izumiya, D. Kurioka, Y. Honma, Y. Yamada, K. Furuta, T. Gunji, H. Ohta, H. Okamoto, H. Sonoda, M. Watanabe, H. Nakagama, J. Yokota, T. Kohno, N. Tsuchiya, *PLoS One* **2014**, *9*, e92921.
 [16] B. K. Thakur, H. Zhang, A. Becker, I. Matei, Y. Huang, B. Costa-Silva, Y. Zheng, A. Hoshino, H. Brazier, J. Xiang, C. Williams, R. Rodriguez-Barrueco, J. M. Silva, W. Zhang, S. Hearn, O. Elemento, N. Paknejad, K. Manova-Todorova, K. Welte, J. Bromberg, H. Peinado, D. Lyden, *Cell Res.* **2014**, *24*, 766.
 [17] G. Rabinowits, C. Gerçel-Taylor, J. M. Day, D. D. Taylor, G. H. Kloecker, *Clin. Lung Cancer* **2009**, *10*, 42.
 [18] J. Woo, S. Sharma, J. Gimzewski, *J. Circ. Biomarkers* **2016**, *5*, 11.
 [19] J. N. Higginbotham, Q. Zhang, D. K. Jeppesen, A. M. Scott, H. C. Manning, J. Ochieng, J. L. Franklin, R. J. Coffey, *J. Extracell. Vesicles* **2016**, *5*, 29254.
 [20] A. A. I. Sina, R. Vaidyanathan, S. Dey, L. G. Carrascosa, M. J. A. Shiddiky, M. Trau, *Sci. Rep.* **2016**, *6*, 30460.
 [21] K. R. Kampen, *J. Membr. Biol.* **2011**, *242*, 69.
 [22] J. P. J. Hegmans, M. P. L. Bard, A. Hemmes, T. M. Luidier, M. J. Kleijmeer, J.-B. Prins, L. Zitvogel, S. A. Burgers, H. C. Hoogsteden, B. N. Lambrecht, *Am. J. Pathol.* **2004**, *164*, 1807.
 [23] R. B. Koumangoye, A. M. Sakwe, J. S. Goodwin, T. Patel, J. Ochieng, *PLoS One* **2011**, *6*, e24234.
 [24] P. T. Caswell, S. Vadrevu, J. C. Norman, *Nat. Rev. Mol. Cell Biol.* **2009**, *10*, 843.
 [25] A. E. Morelli, A. T. Larregina, W. J. Shufesky, M. L. G. Sullivan, D. B. Stolz, G. D. Papworth, A. F. Zahorchak, A. J. Logar, Z. Wang, S. C. Watkins, L. D. Faló, A. W. Thomson, *Blood* **2004**, *104*, 3257.
 [26] S. Rieu, C. Géminard, H. Rabesandratana, J. Sainte Marie, M. Vidal, *Eur. J. Biochem.* **2000**, *267*, 583.
 [27] J. S. Desgrosellier, D. A. Cheresch, *Nat. Rev. Cancer* **2010**, *10*, 9.
 [28] O. H. Aina, *Mol. Cancer Ther.* **2005**, *4*, 806.
 [29] W. Xiao, N. Yao, L. Peng, R. Liu, K. S. Lam, *Eur. J. Nucl. Med. Mol. Imaging* **2009**, *36*, 94.
 [30] L. Peng, R. Liu, J. Marik, X. Wang, Y. Takada, K. S. Lam, *Nat. Chem. Biol.* **2006**, *2*, 381.

- [31] W. Xiao, Y. Wang, E. Y. Lau, J. Luo, N. Yao, C. Shi, L. Meza, H. Tseng, Y. Maeda, P. Kumaresan, R. Liu, F. C. Lightstone, Y. Takada, K. S. Lam, *Mol. Cancer Ther.* **2010**, *9*, 2714.
- [32] K. S. Lam, S. E. Salmon, E. M. Hersh, V. J. Hruby, W. M. Kazmierski, R. J. Knapp, *Nature* **1991**, *354*, 82.
- [33] K. S. Lam, M. Lebl, V. Krchnák, *Chem. Rev.* **1997**, *97*, 411.
- [34] W. Xiao, T. Li, F. C. Bononi, D. Lac, I. A. Kekessie, Y. Liu, E. Sanchez, A. Mazloom, A.-H. Ma, J. Lin, J. Tran, K. Yang, K. S. Lam, R. Liu, *EJNMMI Res.* **2016**, *6*, 18.
- [35] C. Thery, S. Amigorena, G. Raposo, A. Clayton, *Curr. Protoc. Cell Biol.* **2006**, *3*, 22.
- [36] J. Lötvall, A. F. Hill, F. Hochberg, E. I. Buzas, D. Di Vizio, C. Gardiner, Y. S. Gho, I. V. Kurochkin, S. Mathivanan, P. Quesenberry, S. Sahoo, H. Tahara, M. H. Wauben, K. W. Witwer, C. Thery, *J. Extracell. Vesicles* **2014**, *3*, 328.
- [37] J. Webber, A. Clayton, *J. Extracell. Vesicles* **2013**, *2*, 19861.
- [38] Z. J. Smith, C. Lee, T. Rojalín, R. P. Carney, S. Hazari, A. Knudson, K. Lam, H. Saari, E. L. Ibañez, T. Viitala, T. Laaksonen, M. Yliperttula, S. Wachsmann-Hogiu, *J. Extracell. Vesicles* **2015**, *4*, 28533.
- [39] C. Escrevente, S. Keller, P. Altevogt, J. Costa, *BMC Cancer* **2011**, *11*, 108.
- [40] L. Grasso, R. Wyss, L. Weidenauer, A. Thampi, D. Demurtas, M. Prudent, N. Lion, H. Vogel, *Anal. Bioanal. Chem.* **2015**, *407*, 5425.
- [41] K. A. Peterlinz, R. Georgiadis, *Opt. Commun.* **1996**, *130*, 260.
- [42] N. Granqvist, M. Yliperttula, S. Välimäki, P. Pulkkinen, H. Tenhu, T. Viitala, *Langmuir* **2014**, *30*, 2799.
- [43] J. A. De Feijter, J. Benjamins, F. A. Veer, *Biopolymers* **1978**, *17*, 1759.
- [44] E. J. van der Vlist, E. N. M. N.-t. Hoen, W. Stoorvogel, G. J. A. Arkesteijn, M. H. M. Wauben, *Nat. Protoc.* **2012**, *7*, 1311.
- [45] L. Iversen, S. Mathiasen, J. B. Larsen, D. Stamou, *Nat. Chem. Biol.* **2015**, *11*, 822.
- [46] M. Logozzi, A. De Milito, L. Lugini, M. Borghi, L. Calabrò, *PLoS One* **2009**, *4*, e5219.
- [47] S. Fais, L. O'Driscoll, F. E. Borrás, E. Buzas, G. Camussi, F. Cappello, J. Carvalho, A. C. da Silva, H. Del Portillo, S. El-Andaloussi, T. F. Trček, R. Furlan, A. Hendrix, I. Gursel, V. Kralj-Iglic, B. Kaeffer, M. Kosanovic, M. E. Lekka, G. Lipps, M. Logozzi, A. Marcilla, M. Sammar, A. Llorente, I. Nazarenko, C. Oliveira, G. Pocsfalvi, L. Rajendran, G. Raposo, E. Rohde, P. Siljander, G. van Niel, M. H. Vasconcelos, M. Yáñez-Mo, M. L. Yliperttula, N. Zarovni, A. B. Zavec, B. Giebel, *ACS Nano* **2016**, *10*, 3886.
- [48] T. Lener, M. Gimona, L. Aigner, V. Börger, E. Buzas, G. Camussi, N. Chaput, D. Chatterjee, F. A. Court, H. A. del Portillo, L. O'Driscoll, S. Fais, J. M. Falcon-Pérez, U. Felderhoff-Mueser, L. Fraile, Y. S. Gho, A. Görgens, R. C. Gupta, A. Hendrix, D. M. Hermann, A. F. Hill, F. Hochberg, P. A. Horn, D. de Kleijn, L. Kordelas, B. W. Kramer, E.-M. Krämer-Albers, S. Laner-Plamberger, S. Laitinen, T. Leonardi, M. J. Lorenowicz, S. K. Lim, J. Lötvall, C. A. Maguire, A. Marcilla, I. Nazarenko, T. Ochiya, T. Patel, S. Pedersen, G. Pocsfalvi, S. Pluchino, P. Quesenberry, I. G. Reischl, F. J. Rivera, R. Sanzenbacher, K. Schallmoser, I. Slaper-Cortenbach, D. Strunk, T. Tonn, P. Vader, B. W. M. van Balkom, M. Wauben, S. El-Andaloussi, C. Thery, E. Rohde, B. Giebel, *J. Extracell. Vesicles* **2015**, *4*, 30087.
- [49] K. Liang, F. Liu, J. Fan, D. Sun, C. Liu, C. J. Lyon, D. W. Bernard, Y. Li, K. Yokoi, M. H. Katz, E. J. Koay, Z. Zhao, Y. Hu, *Nat. Biomed. Eng.* **2017**, *1*, 0021.
- [50] X. Liu, D. Wu, S. Turgman-Cohen, J. Genzer, T. W. Theyson, O. J. Rojas, *Langmuir* **2010**, *26*, 9565.
- [51] D. L. M. Rupert, C. Lässer, M. Eldh, S. Block, V. P. Zhdanov, J. O. Lötvall, M. Bally, F. Höök, *Anal. Chem.* **2014**, *86*, 5929.
- [52] D. L. M. Rupert, G. V. Shelke, G. Emilsson, V. Claudio, S. Block, C. Lässer, A. B. Dahlin, J. O. Lötvall, M. Bally, V. P. Zhdanov, F. Höök, *Anal. Chem.* **2016**, *88*, 9980.
- [53] M. A. Livshits, E. Khomyakova, E. G. Evtushenko, V. N. Lazarev, N. A. Kulemin, S. E. Semina, E. V. Generozov, V. M. Govorun, *Sci. Rep.* **2015**, *5*, 17319.
- [54] B. D. Beier, *Confocal Raman Microspectroscopy of Oral Streptococci*, Rochester, NY: University of Rochester, **2011**.
- [55] P. H. C. Eilers, *Anal. Chem.* **2003**, *75*, 3631.
- [56] H. F. M. Boelens, R. J. Dijkstra, P. H. C. Eilers, F. Fitzpatrick, J. A. Westerhuis, *J. Chromatogr., A* **2004**, *1057*, 21.
- [57] I. W. Schie, L. Nolte, T. L. Pedersen, Z. Smith, J. Wu, I. Yahiatène, J. W. Newman, T. Huser, *Analyst*, **2013**, *138*, 6662.
- [58] H. Liang, J.-P. Tuppurainen, J. Lehtinen, T. Viitala, M. Yliperttula, *Eur. J. Pharm. Sci.* **2013**, *50*, 492.